Kekulé-induced valley birefringence and skew scattering in graphene

Elias Andrade [1,*] Ramon Carrillo-Bastos [2] Mahmoud M. Asmar [3] and Gerardo G. Naumis [4]

[1]*Posgrado en Ciencias Físicas, Instituto de Física, Universidad Nacional Autónoma de México (UNAM), Apdo. Postal 20-364, 01000 México D.F., México*

[2]*Facultad de Ciencias, Universidad Autónoma de Baja California, Apdo. Postal 1880, 22800 Ensenada, Baja California, México*

[3]*Department of Physics, Kennesaw State University, Marietta, Georgia 30060, USA*

[4]*Depto. de Sistemas Complejos, Instituto de Física, Universidad Nacional Autónoma de México (UNAM), Apdo. Postal 20-364, 01000 México D.F., México*

(Received 8 August 2022; revised 6 October 2022; accepted 1 November 2022; published 14 November 2022)

In graphene, a Kekulé-Y bond texture modifies the electronic band structure, generating two concentric Dirac cones with different Fermi velocities lying in the Γ point in reciprocal space. The energy dispersion results in different group velocities for each isospin component at a given energy. This energy spectrum combined with the negative refraction index in $p-n$ junctions allows the emergence of an electronic analog of optical birefringence in graphene. We characterize the valley birefringence produced by a circularly symmetric Kekulé patterned and gated region using the scattering approach. We found caustics with two cusps separated in space by a distance dependent on the Kekulé interaction and that provides a measure of its strength. Then at low carrier concentration, we find a nonvanishing skew cross-section, showing the asymmetry in the scattering of electrons around the axis of the incoming flux. This effect is associated with the appearance of the valley Hall effect as electrons with opposite valley polarization are deflected toward opposite directions.

DOI: 10.1103/PhysRevB.106.195413

I. INTRODUCTION

The similarities between the Helmholtz and Schrödinger equations result in photons and electrons displaying similar wave phenomena [1]. Furthermore, the propagation of electrons through the two-dimensional honeycomb arrangement of carbon atoms, known as graphene, leads to the dressing of electronic states as massless Dirac-like electronic excitations residing at opposite corners of the Brillouin zone [2], thus augmenting the analogies between the electronic and optical phenomena. The ability to control the charge carrier group velocity via graphene gating [3] has led to the prediction and experimental realization of electronic Veselago lensing, where incoming divergent rays become convergent after refraction on a flat surface with a negative index of refraction [4,5]. The sensitivity of this lensing to the conduction electron properties aids the detection of anisotropies and tilting of the Dirac cones [6,7], the presence of strain [8], and disorder [9]. Veselago lensing also facilitates the waveguiding of electrons in $p-n$ junctions [10,11] and in circular geometries [12] as well as the emergence of caustics (wave envelopes of refracted electrons) which often have cusp singularities. Moreover, like optical birefringence in anisotropic crystals, where the group velocity depends on light polarization [13] and thus incoming light rays can be split in two, spin birefringence for electrons emerges in graphene due to the Rashba spin-orbit interaction [14,15] which leads to distinct Fermi velocities for each spin component. In circular geometries, spin birefringence brings about the formation of caustics with two cusps, with a space separation that depends on the strength of the Rashba spin-orbit coupling [16,17]. However, spin-orbit interactions in graphene are small which makes the detection of spin birefringence experimentally challenging.

In addition to spin, electrons in graphene possess the valley degree of freedom [18]. The valleys in graphene have a large separation in momentum space [19], which suggests that this degree of freedom can be potentially used in applications where it will play a role like spin in spintronics [20,21]. The field that aims to manipulate and control the valley degree of freedom in applications is known as *valleytronics* [22–34]. Like spin-orbit interactions in spintronics, interactions contrasting the degenerate valleys in graphene play an essential role in valleytronincs. Such interactions include the Kekulé patterning of graphene [35,36], i.e., the periodic bond modulation of the graphene lattice. Depending on the bond modulation pattern [37], two different Kekulé distortion phases can emerge: the Kekulé-Y [38] found in graphene deposited on Cu[111] and the Kekulé-O [39–43] that arises in bilayer graphene intercalated with Li. The tight-binding calculations by Gamayun *et al.* [37] found that Kekulé-Y produces an effective interaction that leads to valley-momentum locking, while Kekulé-O leads to the formation of a gap in the electronic spectrum.

Kekulé-Y-patterned graphene breaks a valley degeneracy through valley-momentum locking which produces a low-energy spectrum with two nested Dirac cones with different Fermi velocities [37]. The energy-momentum dispersion modification caused by Kekulé-Y patterning leads to drastic modifications in the magnetic and optical response of

*eandrade@estudiantes.fisica.unam.mx

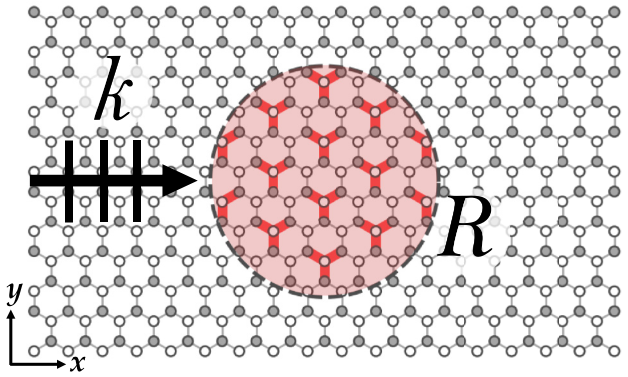

FIG. 1. Schematic of the system (not to scale). A graphene lattice where an incoming flux of electrons in the x direction approaches a circular region of radius R with a gate potential and Kekulé-Y bond texture (red bonds).

graphene [44–49] and crucially aids the control of the valley degree of freedom in the electronic transport [50–57]. In this paper, we study the scattering of Dirac fermions from circularly Kekulé-Y-patterned regions in the semiclassical limit, and we explore the effects of this interaction on electron optics and the appearance of valley birefringence. We also investigate the scattering of charge carriers in graphene from short-range scattering regions with locally enhance Kekulé-Y interactions due to adatom deposition. Our analysis of the total, transport, and skew cross-sections for these short-range scatterers reveals the dependence of these cross-sections on the strength of the Kekulé-Y interaction, and we show the appearance of valley Hall effects due to skew scattering from these scatterers.

The layout of this paper is as follows. In Sec. II, we present the model. Section III is devoted to the scattering calculations. Valley birefringence is analyzed in Sec. IV, while in Sec. V, we study the low-energy scattering. Finally, we conclude by discussing our main findings.

II. MODEL

Our system consists of an infinite sheet of pristine graphene containing a circularly Kekulé-ordered patch of radius R, Fig. 1. We consider the scattering of an incoming flux of electrons in the x direction with momentum k. To describe the electronic properties of the graphene sheet, we adopt the low-energy description, i.e., the Dirac Hamiltonian [19]. Nevertheless, the Kekulé-modulated portion of the lattice has a larger unit cell than the nonmodulated graphene lattice. Hence, to match the pristine and Kekulé-patterned graphene wave functions, it is practical to use an enlarged unitary cell for the case of undistorted graphene. This is equivalent to considering the group C''_{6v}, with a 6-atom graphene unit cell, which avoids the treatment of degenerate states at two inequivalent Dirac points [58]. This is more clearly seen if we start with the Hamiltonian for the Kekulé region, and then pristine graphene appears as a limiting case.

The space-dependent Hamiltonian describing the system in Fig. 1 is given by

$$\mathcal{H} = \mathcal{H}_0 + \mathcal{H}_Y(r) + V(r), \tag{1}$$

where

$$\mathcal{H}_0 = v_f(\mathbf{p}\cdot\boldsymbol{\sigma})\otimes\tau_0 \tag{2}$$

is the low-energy graphene Hamiltonian with $\mathbf{p} = -i\hbar(\partial_x, \partial_y)$ the momentum operator, $v_f \sim 10^6 \mathrm{m/s}$ the Fermi velocity, and σ, τ the sets of Pauli matrices acting on the sublattice and valley pseudospin spaces, respectively. Here,

$$\mathcal{H}_Y = \Delta v_f \sigma_0 \otimes (\mathbf{p}\cdot\boldsymbol{\tau})\Theta(R-r) \tag{3}$$

is the Kekulé-Y bond perturbation [37] with amplitude Δ within the circular region,

$$V(r) = V_0\Theta(R-r)\sigma_0\otimes\tau_0 \tag{4}$$

is a constant gate potential with amplitude V_0 in the Kekulé circular patch, and Θ is the Heaviside function.

The Hamiltonian in Eq. (1) acts on the states expressed in the valley isotropic representation [59]:

$$\Psi = \begin{bmatrix}\psi_{K'}\\ \psi_K\end{bmatrix} = \begin{bmatrix}-\psi_{B,K'}\\ \psi_{A,K'}\\ \psi_{A,K}\\ \psi_{B,K}\end{bmatrix}. \tag{5}$$

Notice that the subindexes A and B in Ψ correspond to each graphene bipartite lattice, while K and K' label the valley. For regions outside the Kekulé-modulated region, the limit of pristine graphene is recovered, $\Delta = 0$, thus having a 4×4 operator which represents the Dirac Hamiltonian in the enlarged unitary cell.

III. SCATTERING

In this section, we study the scattering of Dirac fermions from a circularly symmetric Kekulé-patterned region. We adopt the partial wave-scattering method to find the S-matrix, which requires finding and matching the eigenstates in the different scattering regions of our system. For any effective theory that uses an envelope wave function, as is the case of the Dirac equation for graphene, the matching requires a supplemental boundary condition of the form $\Psi = M\Psi$ to retain the hermiticity and preserve currents. Here, M is a matrix containing the microscopic details and the symmetries of the problem [59–64]. Since we consider the Kekulé-Y bond modulation as a perturbation within the same graphene sheet, no major misalignment is expected, and thus, for small Δ, we can consider M as unitary throughout this paper. Here, we note that we are using a low-energy approximation near the Fermi level for Kekulé-Y graphene. As in pristine graphene, the effective equation is circularly symmetric [37]. At energies away from the Fermi level, the discrete nature of the lattice is initially reflected via trigonal warping. This part of the spectrum is not sampled by fermions near the Fermi energy, as is only visible on other scales of energy. Therefore, we can safely treat our system as circularly symmetric, and thus, it is natural to evaluate its eigenfunctions in polar coordinates. The z component of orbital angular momentum $L_z = -i\hbar\partial_\theta$ does not commute with the Hamiltonian, $[H, L_z] = i\hbar v_f(\boldsymbol{\sigma}\times\mathbf{p})_z\otimes\tau_0 + i\hbar v_f\sigma_0\otimes(\boldsymbol{\tau}\times\mathbf{p})_z$. On the other hand, the sum of L_z and the intrinsic angular momenta associated with the valley and sublattice degrees of freedom, *valley-lattice-angular momentum* J_z, is conserved and given by

$$J_z = L_z + \frac{\hbar}{2}(\sigma_z \otimes \tau_0 + \sigma_0 \otimes \tau_z). \tag{6}$$

Here, it is important to notice that $(H, \frac{\hbar}{2}\sigma_z \otimes \tau_0) = -i\hbar v_f(\boldsymbol{\sigma} \times \mathbf{p})_z \otimes \tau_0$, and $(H, \frac{\hbar}{2}\sigma_0 \otimes \tau_z) = -i\hbar v_f \sigma_0 \otimes (\boldsymbol{\tau} \times \mathbf{p})_z$, which leads to $(H, \frac{\hbar}{2}\sigma_z \otimes \tau_0 + \frac{\hbar}{2}\sigma_0 \otimes \tau_z + L_z) = 0$. We can express the eigenfunctions in their total pseudo-angular momentum basis, such that $J_z\Psi_m = m\hbar\Psi_m$; thus,

$$\Psi_m(r,\theta) = \exp(im\theta)\begin{bmatrix} -\exp(-i\theta)\Phi_{B,K'}(r) \\ \Phi_{A,K'}(r) \\ \Phi_{A,K}(r) \\ \exp(i\theta)\Phi_{B,K}(r) \end{bmatrix}, \tag{7}$$

where $\theta = \tan^{-1} y/x$, and we find the radial part of the wave functions by applying the Hamiltonian in Eq. (1) to our spinor in Eq. (7) to get the following set of coupled differential equations:

$$L_m^-[\Phi_{A,K'}(r) + \Delta\Phi_{A,K}(r)] = -i(\epsilon - \nu)\Phi_{B,K'}(r), \tag{8a}$$

$$L_{m-1}^+\Phi_{B,K'}(r) - \Delta L_{m+1}^-\Phi_{B,K}(r) = -i(\epsilon - \nu)\Phi_{A,K'}(r), \tag{8b}$$

$$L_{m+1}^-\Phi_{B,K}(r) - \Delta L_{m-1}^+\Phi_{B,K'}(r) = i(\epsilon - \nu)\Phi_{A,K}(r), \tag{8c}$$

$$L_m^+[\Phi_{A,K}(r) + \Delta\Phi_{A,K'}(r)] = i(\epsilon - \nu)\Phi_{B,K}(r), \tag{8d}$$

where

$$L_m^{\pm} = \left(\partial_r \mp \frac{m}{r}\right). \tag{8e}$$

Here, $\epsilon = E/(\hbar v_f)$ and $\nu = V_0/(\hbar v_f)$. Since $L_m^{\pm}$ acts as a ladder operator for the cylindrical Bessel functions J_m,

$$L_m^{\pm}J_m(kr) = \mp kJ_{m\pm1}(kr); \tag{9}$$

thus, a natural ansatz is

$$\Phi_{A,K}(r) = i(\epsilon - \nu)C_A J_m(kr), \tag{10}$$

$$\Phi_{A,K'}(r) = i(\epsilon - \nu)C_B J_m(kr), \tag{11}$$

where C_A and C_B are constants, and k is the electron wave number. Inserting the ansatz in Eq. (10) into the relations in Eqs. (8a)–(8e) results in the exact form of the spinor solutions and determines the wave numbers:

$$k_{\pm} = \frac{|E - V_0|}{\hbar v_f(1 \pm \Delta)}. \tag{12}$$

Thus, the mth angular momentum eigenstates in the inner region are

$$\Psi_m^{(\text{inner})}(r,\theta) = T_m^+\exp(im\theta)\begin{bmatrix} J_{m-1}(k_+r)\exp(-i\theta) \\ is'J_m(k_+r) \\ is'J_m(k_+r) \\ -J_{m+1}(k_+r)\exp(i\theta) \end{bmatrix} + T_m^-\exp(im\theta)\begin{bmatrix} J_{m-1}(k_-r)\exp(-i\theta) \\ is'J_m(k_-r) \\ -is'J_m(k_-r) \\ J_{m+1}(k_-r)\exp(i\theta) \end{bmatrix}, \tag{13}$$

where T_m^+ and T_m^- are determined by $s' = \text{sgn}(E - V_0)$ and the boundary conditions. Since the pseudo-angular momentum is conserved during the scattering process, we can treat each component of m independently and use the partial wave method to determine the S-matrix elements. In the region $r > R$, we describe the wave function in terms of incoming (in) and outgoing (out) cylindrical waves, where the corresponding spinor for each valley is

$$\psi_{m,K'}^{(\text{out})/(\text{in})}(r,\theta)\,|K'\rangle = \begin{Bmatrix} H_{m-1}^{(1)/(2)}(kr)\exp[i(m-1)\theta] \\ isH_m^{(1)/(2)}(kr)\exp(im\theta) \end{Bmatrix}|K'\rangle, \tag{14a}$$

$$\psi_{m,K}^{(\text{out})/(\text{in})}(r,\theta)\,|K\rangle = \begin{Bmatrix} -isH_m^{(1)/(2)}(kr)\exp(im\theta) \\ H_{m+1}^{(1)/(2)}(kr)\exp[i(m+1)\theta] \end{Bmatrix}|K\rangle, \tag{14b}$$

$$|K'\rangle = \begin{pmatrix} 1 \\ 0 \end{pmatrix}, \quad |K\rangle = \begin{pmatrix} 0 \\ 1 \end{pmatrix}. \tag{14c}$$

Here, $|K\rangle$ and $|K'\rangle$ are valley spinors, $H_m^{(1)}$ and $H_m^{(2)}$ are Hankel functions of the first and second kind, respectively, and $s = \text{sgn}(E)$. Now we can write the wave functions in terms of the scattering matrix S_m such that $\psi_m = \psi_m^{(\text{in})} + S_m\psi_m^{(\text{out})}$:

$$\Psi_m^{(\text{outer})}(r,\theta) = \sum_\alpha c_\alpha \psi_{m,\alpha}^{(\text{in})}(r,\theta)\,|\alpha\rangle + \sum_{\alpha,\beta} c_\alpha S_{m,\alpha\beta}\psi_{m,\beta}^{(\text{out})}(r,\theta)\,|\beta\rangle, \tag{15}$$

where $\alpha = K, K'$ and $\beta = K, K'$ are valley indexes. The symbol $S_{m,\alpha\beta}$ denotes the scattering from α to β valley, c_K and $c_{K'}$ are the weights of the valley polarization. We can obtain the coefficients for S_m, T_m^+, and T_m^- by applying the boundary conditions at $\Psi_m^{(\text{inner})}(R,\theta) = \Psi_m^{(\text{outer})}(R,\theta)$, as shown in Appendix. Additionally, an incident plane-wave in the x direction can be expressed with the aid of the Jacobi-Anger expansion as

$$\exp(ikr\cos\theta) = \sum_{m=-\infty}^{\infty} i^n J_m(kr)\exp(im\theta), \tag{16}$$

or equivalently as

$$\Phi_0(r,\theta) = \sum_{m=-\infty}^{\infty}\sum_\alpha c_\alpha \frac{i^m}{2}\left[\psi_{m,\alpha}^{(\text{out})}(r,\theta) + \psi_{m,\alpha}^{(\text{in})}(r,\theta)\right]|\alpha\rangle. \tag{17}$$

The latter allows one to express $\Psi^{(\text{outer})}(r,\theta)$ in terms of the incoming plane and the outgoing waves, i.e.,

$$\Psi^{(\text{outer})}(r,\theta) = \Phi_0(r,\theta) + \sum_{m=-\infty}^{\infty}\sum_{\substack{\alpha=K,K' \\ \bar{\alpha}\neq\alpha}} \times c_\alpha \frac{i^m}{2}\left[(S_{m,\alpha\alpha} - 1)\psi_{m,\alpha}^{(\text{out})}(r,\theta)\,|\alpha\rangle + S_{m,\alpha\bar{\alpha}}\psi_{m,\bar{\alpha}}^{(\text{out})}(r,\theta)\,|\bar{\alpha}\rangle\right], \tag{18}$$

and the total wave function is obtained by

$$\Psi(r,\theta) = \sum_{m=-\infty}^{\infty}\left[\Psi_m^{(\text{inner})}(r,\theta) + \Psi_m^{(\text{outer})}(r,\theta)\right]. \tag{19}$$

IV. VALLEY BIREFRINGENCE

Partially subjecting a graphene sheet to a gate potential that reverses its carrier character from electrons to holes between gated and nongated regions leads to many interesting analogies between its electron dynamics and optical phenomena [4,12,16]. The key ingredient to this phenomena is the reversal of the group velocity of quasiparticles between the regions with and without gate potentials. For example and to visualize the phenomena, we consider that the Fermi level of the system is $E_{\mathrm{F}} > 0$, such that, for the outer region, it crosses the upper band. On the hand, in the inner region, $E_{\mathrm{F}} - V_0 < 0$, with $V_0 > 0$, which means that the Fermi level crosses the lower band. In this case (Fig. 1, with $\Delta_0 = 0$), for $r > R$, the group velocity of the quasiparticle is parallel to the wave vector, i.e., $v_g^{(\mathrm{outer})} = v_f[k_{x,r^{(\mathrm{outer})}}\hat{x} + k_{y,r^{(\mathrm{outer})}}\hat{y}]/|k_{r^{(\mathrm{outer})}}|$. In the inner region, it is antiparallel $v_g^{(\mathrm{inner})} = -v_f[k_{x,r^{(\mathrm{inner})}}\hat{x} + k_{y,r^{(\mathrm{inner})}}\hat{y}]/|k_{r^{(\mathrm{inner})}}|$. Here, $k_{r^{(\mathrm{inner})}}$ $[k_{r^{(\mathrm{outer})}}]$ is the wave vector in the inner (outer) region. Since the group velocity is $v_g = dE(k)/d(\hbar k)$, if k is kept fixed, the sign of $E(k)$ changes for the valence and conduction bands, making it parallel to the Fermi momentum for n-type carriers but antiparallel for p-type [65].

The reversal of the group velocity from the outer to the inner region indicates that the gated region will act, in the semiclassical limit, as a circular electronic lens with a negative index of refraction $n = -k_{r^{(\mathrm{inner})}}/k_{r^{(\mathrm{outer})}}$, where $k_{r^{(\mathrm{inner})}}$ is the wave number inside the gated patch and $k_{r^{(\mathrm{outer})}}$ outside, and n is deduced from the electronic Snell's law [4,18]. As shown in Fig. 1, in the limit $kR \gg 1$, the negative index of refraction leads to constructive interference between the different partial wave components and results in a probability density that forms cardioid caustics and cusps [12], in what mimics the optical caustics which arise from light refraction through a shaped medium and belong to a class of cusps in catastrophe theory [13]. Using differential geometry [12], the positions of the cusps for each $p-1$ internal reflection can be shown to be

$$x_{\mathrm{cusp}}(p) = \frac{(-1)^p}{|n| - 1 + 2p}R, \tag{20}$$

and in the case shown in Fig. 2(a), as the amplitude decreases with each internal reflection, we can clearly distinguish the cusps corresponding to $p = 1, 2$.

If in addition to the gate potential the circular region contains the Kekulé bond texture, then the electronic bands in this region will be characterized by $E_\pm = \pm\hbar v_f(1 \pm \Delta)|\mathbf{k}| + V_0$. Therefore, the gating of this region leads to the Fermi level intersecting the two degenerate bands, which are characterized by the two group velocities $v_{g,\pm} = -v_f(1 \pm \Delta)$. Then when $\Delta \neq 0$, in addition to the sign reversal of the group velocity between both regions, we also have the two different group velocities in the inner region. Hence, the Kekulé patterned and gated region will act as a circular lens with two negative indices of refraction:

$$n_\pm = -\frac{k_{\pm,r^{(\mathrm{inner})}}}{k_{r^{(\mathrm{outer})}}}, \tag{21}$$

with $k_{\pm,r^{(\mathrm{inner})}} = k_+, k_-$, which are given in Eq. (12). As shown in Fig. 2(b), the Kekulé patterning of the circular region results in the doubling of the cusps and caustics of the circular lens, which reflects its birefringent nature. The degree of birefringence can be characterized by $\zeta = |n_+ - n_-|$, and for the set of parameters in Fig. 2(b), we get $\zeta \approx 0.25$. Moreover, the cusp location is now modified to

$$x^\pm_{\mathrm{cusp}}(p) = \frac{(-1)^p}{|n_\pm| - 1 + 2p}R, \tag{22}$$

and the spatial separation between the two cusps is found by $|x^+_{\mathrm{cusp}} - x^-_{\mathrm{cusp}}|$. In Fig. 2(c), we show the valley-preserving amplitude component $|\psi_{K'K'}(r)|^2$, which retains the same valley component as the incoming electrons and, in Fig. 2(d), the valley-mixing component $|\psi_{K'K}(r)|^2$, which flips the valley degree of freedom. From these figures, we can notice that the Kekulé bond texture leads to the oscillation of the valley component as electrons travel in the patterned region, in what mimics the spin-momentum coupling of the electron in the presence of a Rashba interaction [14,16].

V. LOW-ENERGY SCATTERING

The scattering process can be further analyzed by obtaining the different types of cross-sections, such as the total cross-section σ_t, which tells us the magnitude of the interaction between the incoming flux and the scattering region, the transport cross-section σ_{tr} that describes the average momentum transfer during the scattering, and the skew cross-section σ_{sk}, which shows the asymmetry in the scattering around the axis of the incoming flux. These quantities can be obtained through the scattering amplitude $f(\theta)$, which can be found in the far field limit, i.e., via the asymptotic form of the wave function as $r \to \infty$:

$$\Psi(r \to \infty) \to \Phi_0 + \sum_m \sum_{\alpha,\beta} c_\alpha f_{m,\alpha\beta}(\theta)\frac{\exp(ikr)}{\sqrt{r}}\,|\beta\rangle\,, \tag{23}$$

and using the asymptotic expansion of the Hankel functions:

$$H_m(kr)^{(1)/(2)} \to \sqrt{\frac{2}{\pi kr}}\exp\left[\pm i\left(kr - \frac{m\pi}{2} - \frac{\pi}{4}\right)\right]. \tag{24}$$

By comparing Eqs. (18) and (23), we can deduce the scattering amplitude for each partial wave component in terms of the S-matrix components:

$$f_m = \frac{\exp\left(-\frac{i\pi}{4}\right)}{\sqrt{2\pi k}}\begin{pmatrix} S_{m,K',K'} - 1 & -iS_{m,K',K} \\ iS_{m,K,K'} & S_{m,K,K} - 1\end{pmatrix}, \tag{25}$$

where $S_{m,\alpha\beta}$ are the valley-preserving $(\alpha = \beta)$ and valley-mixing scattering $(\alpha \neq \beta)$ matrix elements corresponding to the mth partial wave component (α and β represent the Dirac points, either K or K'). Then for each process (valley preserving and valley mixing), we find the corresponding differential cross-section:

$$\sigma_{\alpha\beta}(\theta) = \left|\sum_{m=-\infty}^{\infty} f_{m,\alpha\beta}\exp(im\theta)\right|^2, \tag{26}$$

total cross-section:

$$\sigma_{t,\alpha\beta} = \int_{-\pi}^{\pi}\sigma_{\alpha\beta}(\theta)d\theta = 2\pi\sum_{m=-\infty}^{\infty}|f_{m,\alpha\beta}|^2, \tag{27}$$

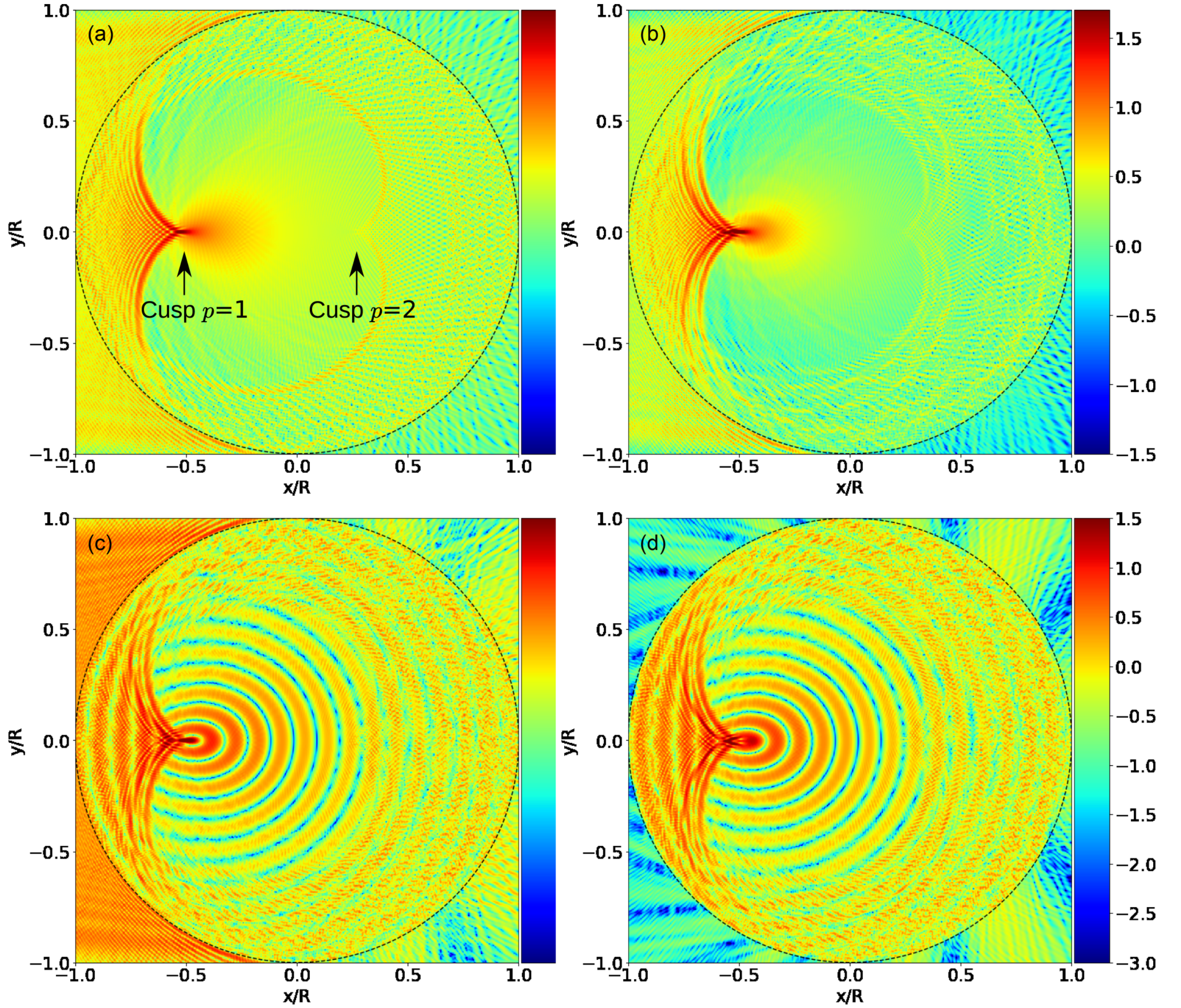

FIG. 2. Space dependence of the probability density (in $\log_{10}$ scale), for an incoming electron flux in the x direction with valley polarization K' and $kR = 300$. The dashed line shows the boundary between the scattering regions. A gate potential $V_0R/(\hbar v_f) = 600$ is present in the inner region. (a) Pristine graphene and (b) Kekulé-Y distorted graphene in the $r < R$ region with $\Delta = 0.1$. The negative refractive index in addition to the circular geometry leads to an interference pattern that forms a cardioid-shaped envelope with a high concentration at the cusps, which split in two as we turn on the Kekulé distortion. The position of the cups is given by Eqs. (20) and (22) for the cases of (a) and (b), respectively. (c) Valley-preserving component and (d) valley-flip component for the case described in (b). As the incoming electron enters the circular region, its valley state begins to oscillate between K and K' [(c) and (d)]. The wavelength of the oscillation depends on the amplitude of Δ, as this parameter characterizes the wave numbers k_+ and k_-.

transport cross-section:

$$\sigma_{tr,\alpha\beta} = \int_{-\pi}^{\pi} \sigma_{\alpha\beta}(\theta)(1-\cos\theta)d\theta$$
$$= \sigma_{t,\alpha\beta} - 2\pi \sum_{m=-\infty}^{\infty} \mathrm{Re}(f_{m,\alpha\beta}f^*_{m+1,\alpha\beta}), \tag{28}$$

and the skew cross-section:

$$\sigma_{sk,\alpha\beta} = \int_{-\pi}^{\pi} \sigma_{\alpha\beta}(\theta)\sin\theta d\theta = 2\pi \sum_{m=-\infty}^{\infty} \mathrm{Im}(f_{m,\alpha\beta}f^*_{m+1,\alpha\beta}). \tag{29}$$

By summing over all different allowed processes:

$$\sigma_\eta = \sum_{\alpha,\beta} \sigma_{\eta,\alpha\beta}, \tag{30}$$

we obtain the total, transport, and skew cross-sections ($\eta \in \{t, tr, sk\}$).

For low carrier concentrations and small regions with Kekulé bond texture ($kR \ll 1$), the most significant scattering channels are those of angular momentum $m = -1, 0, 1$. Within this regime, we show in Fig. 3 the total cross-section against the strength of gate potential V_0. In the absence of Kekulé patterning, the total cross-section of the gated region displays one peak which uniquely arises from the

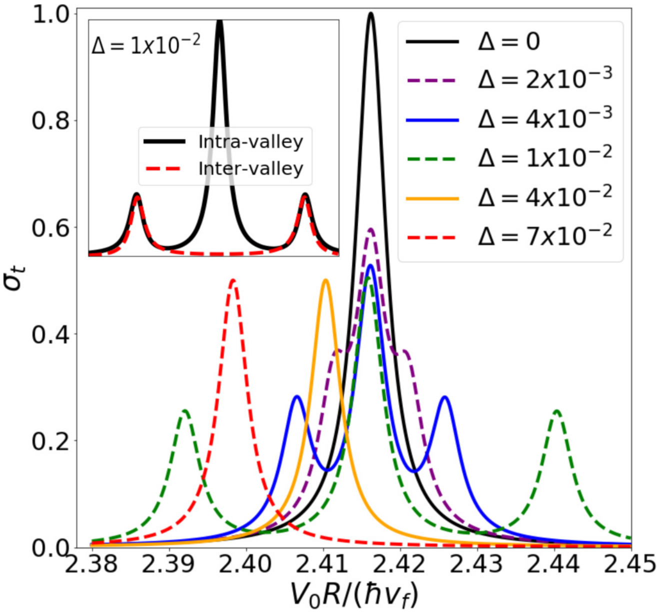

FIG. 3. Total cross-section σ_t as a function of V_0 for incoming electrons in the x direction with $kR = 1.5 \times 10^{-3}$. In the regime $kR \ll 1$, the resonances appear near the zeros of J_0. Here, we show the resonances around the first one $\kappa_0^1 = 2.4048$ [see Appendix, Eq. (A2a)]. (Inset) Total cross-section for intravalley $\sigma_{t,KK} + \sigma_{t,K'K'}$ and intervalley $\sigma_{t,KK'} + \sigma_{t,K'K}$ processes with $\Delta = 0.01$. To present the evolution of the intervalley peaks, this figure only contains a zoom around the $\Delta = 0$ peak. Notice that the valley-mixing peaks are not shown in the figure for the largest two Δ values. These peaks are out of the figure range since Δ shifts to the intervalley peak and increases its separation from the intravalley peaks.

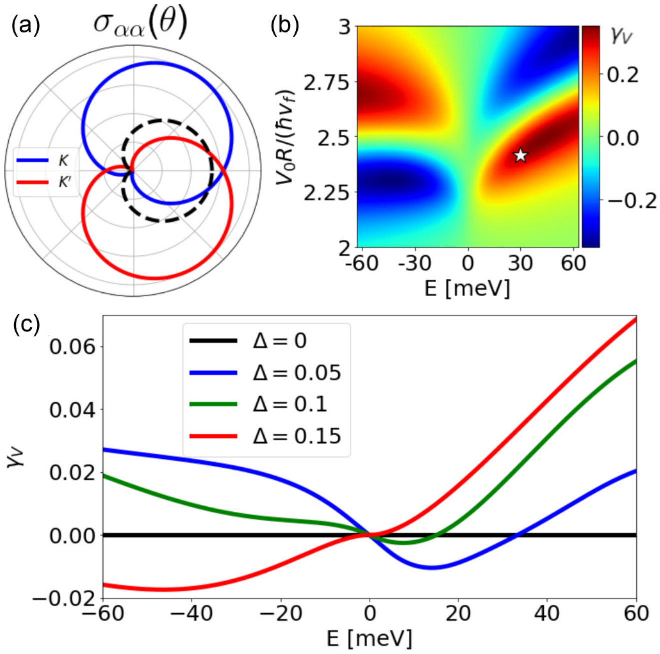

FIG. 4. (a) Differential cross-section for valley-preserving processes, K valley (blue) and K' valley (red), showing the tilt of electrons with opposite valley-polarization toward opposite directions around the x axis. The dashed black line in (a) corresponds to the differential cross-section without Kekulé distortion. (b) Valley skew parameter γ_V as a function of both energy and the gate potential for a region of $R = 9$ Å and Kekulé amplitude $\Delta = 0.1$. The star marker indicates the values used for (a). (c) Average of γ_V as a function of energy for 4000 randomly sized Kekulé-Y regions ($9 \leqslant R \leqslant 18$) Å, considering $V = 1$ eV and different values of Δ.

valley-preserving process and indicates the formation of quasibound states in this region with finite lifetime characterized by the width of the peak [17,66]. An increasing strength of the Kekulé interaction leads to the central (valley-preserving) peak height shrinking and its location shifting, while two new resonant (valley-mixing) peaks emerge. These two new peaks correspond to quasibound states forming due to valley-mixing processes, as shown in the inset of Fig. 3, and consequently, their height increases with increasing values of Δ, as shown in Fig. 3.

When local interactions in a graphene sheet lead to the breaking of effective time reversal (time reversal per valley) while preserving the total time reversal, as is the case for the Kekulé patterning, it is possible to have a skew scattering, and by symmetry considerations, it can be shown that [17]

$$\sigma_{sk,\alpha\alpha} = -\sigma_{sk,\bar{\alpha}\bar{\alpha}}, \tag{31a}$$

$$\sigma_{sk,\alpha\bar{\alpha}} = 0. \tag{31b}$$

The latter equations indicate that electrons with opposite valley polarization get deflected toward opposite directions as they get scattered, thus producing a valley Hall effect. To measure the asymmetry of the scattering per valley, we calculate the skew parameter γ_V, which is defined as

$$\gamma_V = \tfrac{1}{2}(\gamma_K - \gamma_{K'}), \tag{32}$$

where the skew parameter for a valley $\beta = K$ or $\beta = K'$ is

$$\gamma_\beta = \frac{\sum_\alpha \sigma_{sk,\alpha\beta}}{\sum_\alpha \sigma_{tr,\alpha\beta}}. \tag{33}$$

This quantity is directly connected to the transverse valley currents and is equal to the valley Hall angle at zero temperature in the absence of side-jump effects [67]:

$$\Theta_{VH} = \frac{j_{VH}}{j_x} = \gamma_V. \tag{34}$$

In the presence of the Kekulé-Y modulation, the valley asymmetry of scattering around the x axis can also be deduced from the valley-dependent differential cross-section. In Fig. 4(a), we present the differential cross-section per valley for the set of parameters indicated by a star marker in Fig. 4(b). In contrast, we notice a symmetric scattering in the absence of the Kekulé-Y modulation, which is shown by the dashed black line in Fig. 4(a). To show the dependence of the skew scattering in our system on the local potential of the Kekulé-Y-patterned patches V_0 and the Fermi energy (E), in Fig. 4(b), we show a map of the skew parameter γ_V as a function of V_0 and E for Kekulé-patterned regions with $R = 9$ Å and $\Delta = 0.1$. In the latter, we should note that the regions of high γ_V coincide with the regions of resonant scattering, i.e., the resonant regime in the total cross-section (Fig. 3), which indicates that skew scattering is resonantly enhanced [67]. To demonstrate the robustness of skew scattering in the system to variations in size of the Kekulé-Y-patterned patches, we consider a uniform random distribution of impurity sizes in the dilute limit. In Fig. 4(c), we show the average of γ_V for different values of Δ and V_0. Since skew scattering is resonantly enhanced, then its detection survives the random variations in the sizes of the Kekulé-patterned patches in the dilute limit, which allows for the detection of valley Hall effect signatures in transport experiments. We also note that, since $RV_0/(\hbar v_f)$ governs the appearance of the different scattering regimes in Fig. 3, then skew scattering is also robust to variations in the locally enhanced potential.

Let us briefly discuss a suitable set of parameters. Here, Δ is fixed by the Kekulé pattern bond modulation, which we will suppose as others [37] of order $\Delta \approx 0.1$; although, in principle, its value can be varied by applying strain [41,68], a way to determine this parameter is by modeling the Kekulé lattice using a density functional theory approach and obtaining an effective tight-binding model. The experimental setup can vary the two parameters V_0 and R. For example, in Fig. 4, we present the results for patches of size $R = 9$ Å, which is the minimal size to have multiple unit cells in the patch regions, so we can still apply our low-energy continuum model; values above that will be also valid. From the figure, we see that detection will involve the condition $V_0R/\hbar v_f \approx 2.42$, from which we obtain a gate voltage of ~0.66 eV. From there, V_0 can be diminished at will.

VI. CONCLUSIONS

We have studied the scattering of Dirac fermions from Kekulé-distorted and gated regions in graphene. For large Kekulé-patterned and gated regions, we have shown that the scattering of electrons from these circular patches leads to the formation of caustics and cusps reminiscent of a circular birefringent electronic lens with two negative indices of refraction. Moreover, the separation of the cusps in the circular lens is proportional to the Kekulé interaction and provides a direct measure of its strength in systems with tailored Kekulé patches.

For low carrier concentrations, we have shown that the presence of scatterers with a locally enhanced Kekulé interaction and gate potential leads to the electrons from different valleys deflecting in opposite directions due to the skew scattering produced by the Kekulé distortion. Skew scattering in the system leads to the appearance of a valley Hall effect. We have also shown that the skew-scattering-generated valley Hall effect can be present in systems where the Kekulé patterning is not uniform but when it consists of patches with random sizes and potentials. The latter suggests the plausible experimental realization and detection of the skew-scattering-induced valley Hall effect in Kekulé-patterned graphene systems via four-probe experiments. Also, it may be worth extending this study to other short-wavelength modulations, for example, for $\sqrt{3} \times \sqrt{3}$ superlattices and twisted multilayered graphene [69].

Therefore, valley birefringence directly measures the presence of Kekulé-Y distortion, and its strength relates to wavefront separation at the cusps. In the case of low-carrier concentrations, the combination of Kekulé distortion and gate potential can lead to an asymmetric scattering between valleys and thus produce a valley Hall effect, even if the Kekulé pattern is not uniform.

Optical birefringence allows the identification of internal anisotropies, stresses, and space inhomogeneities of materials and even allows decoupling polarized modes in optical fibers. Consequently, our results could serve to design configurations that discern broken symmetries and thus be used to design valley-decoupled electronic analogs to optical fibers.

ACKNOWLEDGMENTS

E.A. and R.C.-B. acknowledge useful discussions with Alex Santacruz. This paper was supported by UNAM Dirección General Asuntos del Personal Académico Programa de Apoyo a Proyectos de Investigación e Innovación Tecnológica IN102620 (E.A. and G.G.N.), Consejo Nacional de Ciencia y Tecnología Project No. 1564464 (E.A. and G.G.N.), and the National Science Foundation via Grant No. DMR-2213429 (M.M.A.).

APPENDIX: BOUNDARY CONDITIONS

In this Appendix, we find explicit solutions for the coefficients in Sec. III, which are found by solving for the boundary conditions. The solution of the system of equations resulting from the boundary condition $\Psi_m^{(\text{inner})}(R,\theta) = \Psi_m^{(\text{outer})}(R,\theta)$ gives us the following analytical expressions for the S_m matrix element s and the amplitudes $T_m^{\pm}$:

$$S_{m,K'K'} = \frac{ss'\big[H_m^{(1)}H_{m-1}^{(2)}X_m + H_{m+1}^{(1)}H_m^{(2)}X_{m-1}\big]}{D_m} - \frac{2H_{m+1}^{(1)}H_{m-1}^{(2)}Q_m + H_m^{(1)}H_m^{(2)}Z_m}{D_m}, \tag{A1a}$$

$$S_{m,KK} = \frac{ss'\big[H_{m-1}^{(1)}H_m^{(2)}X_m + H_m^{(1)}H_{m+1}^{(2)}X_{m-1}\big]}{D_m} - \frac{2H_{m-1}^{(1)}H_{m+1}^{(2)}Q_m + H_m^{(1)}H_m^{(2)}Z_m}{D_m}, \tag{A1b}$$

$$S_{m,K'K} = \frac{-ss'Y_mP_m}{D_m}, \tag{A1c}$$

$$S_{m,KK'} = \frac{-ss'Y_{m-1}P_{m+1}}{D_m}, \tag{A1d}$$

$$T_m^+ = \frac{c_1\big[j_{m+1}^-H_m^{(1)} - ss'\,j_m^-H_{m+1}^{(1)}\big]P_m}{D_m} + \frac{c_2\big[j_{m-1}^-H_m^{(1)} - ss'\,j_m^-H_{m-1}^{(1)}\big]P_{m+1}}{D_m}, \tag{A1e}$$

$$T_m^- = \frac{c_1\big[j_{m+1}^+H_m^{(1)} - ss'\,j_m^+H_{m+1}^{(1)}\big]P_m}{D_m} - \frac{c_2\big[j_{m-1}^+H_m^{(1)} - ss'\,j_m^+H_{m-1}^{(1)}\big]P_{m+1}}{D_m}, \tag{A1f}$$

where we defined

$$D_m = -ss'\left[H_m^{(1)}H_{m-1}^{(1)}X_m + H_{m+1}^{(1)}H_m^{(1)}X_{m-1}\right] + 2H_{m+1}^{(1)}H_{m-1}^{(1)}Q_m + H_m^{(1)}H_m^{(1)}Z_m, \tag{A2a}$$

$$X_m = j_m^+ j_{m+1}^- + j_{m+1}^+ j_m^-, \tag{A2b}$$

$$Y_m = j_m^+ j_{m+1}^- - j_{m+1}^+ j_m^-, \tag{A2c}$$

$$Z_m = j_{m-1}^+ j_{m+1}^- + j_{m+1}^+ j_{m-1}^-, \tag{A2d}$$

$$Q_m = j_m^+ j_m^-, \tag{A2e}$$

$$P_m = H_m^{(1)}H_{m-1}^{(2)} - H_{m-1}^{(1)}H_m^{(2)}. \tag{A2f}$$

Here, all Hankel functions are evaluated at kR and $j_m^{\pm} = J_m(k_{\pm}R)$.

[1] D. Dragoman and M. Dragoman, *Quantum-Classical Analogies* (Springer, Berlin, Heidelberg, 2004).
[2] M. Katsnelson, K. Novoselov, and A. Geim, Nat. Phys. **2**, 620 (2006).
[3] K. S. Novoselov, A. K. Geim, S. V. Morozov, D. Jiang, Y. Zhang, S. V. Dubonos, I. V. Grigorieva, and A. A. Firsov, Science **306**, 666 (2004).
[4] V. V. Cheianov, V. Fal'ko, and B. Altshuler, Science **315**, 1252 (2007).
[5] G.-H. Lee, G.-H. Park, and H.-J. Lee, Nat. Phys. **11**, 925 (2015).
[6] S.-H. Zhang, W. Yang, and F. M. Peeters, Phys. Rev. B **97**, 205437 (2018).
[7] S.-H. Zhang and W. Yang, New J. Phys. **21**, 103052 (2019).
[8] Y. Betancur-Ocampo, Phys. Rev. B **98**, 205421 (2018).
[9] F. Libisch, T. Hisch, R. Glattauer, L. A. Chizhova, and J. Burgdörfer, J. Phys.: Condens. Matter **29**, 114002 (2017).
[10] J. Williams, T. Low, M. Lundstrom, and C. Marcus, Nat. Nanotechnol. **6**, 222 (2011).
[11] Y. Betancur-Ocampo, F. Leyvraz, and T. Stegmann, Nano Lett. **19**, 7760 (2019).
[12] J. Cserti, A. Pályi, and C. Péterfalvi, Phys. Rev. Lett. **99**, 246801 (2007).
[13] M. Berry and C. Upstill, *Progress in Optics* (Elsevier, Amsterdam, 1980), Vol. 18, pp. 257–346.
[14] Yu. A. Bychkov and É. I. Rashba, Pis'ma Zh. Eksp. Toer. Fiz. **39**, 66 (1984) [JETP Lett. **39**, 78 (1984)].
[15] C. L. Kane and E. J. Mele, Phys. Rev. Lett. **95**, 226801 (2005).
[16] M. M. Asmar and S. E. Ulloa, Phys. Rev. B **87**, 075420 (2013).
[17] M. M. Asmar and S. E. Ulloa, Phys. Rev. B **91**, 165407 (2015).
[18] A. H. Castro Neto, F. Guinea, N. M. R. Peres, K. S. Novoselov, and A. K. Geim, Rev. Mod. Phys. **81**, 109 (2009).
[19] M. I. Katsnelson and M. I. Katsnelson, *Graphene: Carbon in Two Dimensions* (Cambridge University Press, Cambridge, 2012).
[20] V. K. Joshi, Eng. Sci. Technol. Int. J. **19**, 1503 (2016).
[21] I. Žutić, J. Fabian, and S. Das Sarma, Rev. Mod. Phys. **76**, 323 (2004).
[22] A. Rycerz, J. Tworzydło, and C. W. J. Beenakker, Nat. Phys. **3**, 172 (2007).
[23] D. Gunlycke and C. T. White, Phys. Rev. Lett. **106**, 136806 (2011).
[24] J.-H. Chen, G. Autès, N. Alem, F. Gargiulo, A. Gautam, M. Linck, C. Kisielowski, O. V. Yazyev, S. G. Louie, and A. Zettl, Phys. Rev. B **89**, 121407(R) (2014).
[25] Y. Liu, J. Song, Y. Li, Y. Liu, and Q.-F. Sun, Phys. Rev. B **87**, 195445 (2013).
[26] Z. Liu, L. Jiang, and Y. Zheng, J. Phys.: Condens. Matter **27**, 045501 (2015).
[27] F. Zhai, X. Zhao, K. Chang, and H. Q. Xu, Phys. Rev. B **82**, 115442 (2010).
[28] M. Ramezani Masir, A. Matulis, and F. M. Peeters, Phys. Rev. B **84**, 245413 (2011).
[29] D. Moldovan, M. Ramezani Masir, L. Covaci, and F. M. Peeters, Phys. Rev. B **86**, 115431 (2012).
[30] J. Wang and S. Fischer, Phys. Rev. B **89**, 245421 (2014).
[31] J. L. Garcia-Pomar, A. Cortijo, and M. Nieto-Vesperinas, Phys. Rev. Lett. **100**, 236801 (2008).
[32] Y. Jiang, T. Low, K. Chang, M. I. Katsnelson, and F. Guinea, Phys. Rev. Lett. **110**, 046601 (2013).
[33] M. M. Grujić, M. Tadić, and F. M. Peeters, Phys. Rev. Lett. **113**, 046601 (2014).
[34] M. M. Asmar and S. E. Ulloa, Phys. Rev. B **96**, 201407(R) (2017).
[35] C.-Y. Hou, C. Chamon, and C. Mudry, Phys. Rev. Lett. **98**, 186809 (2007).
[36] C. Chamon, Phys. Rev. B **62**, 2806 (2000).
[37] O. Gamayun, V. Ostroukh, N. Gnezdilov, I. Adagideli, and C. Beenakker, New J. Phys. **20**, 023016 (2018).
[38] C. Gutiérrez, C.-J. Kim, L. Brown, T. Schiros, D. Nordlund, E. B. Lochocki, K. M. Shen, J. Park, and A. N. Pasupathy, Nat. Phys. **12**, 950 (2016).
[39] C. Bao, H. Zhang, T. Zhang, X. Wu, L. Luo, S. Zhou, Q. Li, Y. Hou, W. Yao, L. Liu *et al.*, Phys. Rev. Lett. **126**, 206804 (2021).
[40] C. Bao, H. Zhang, X. Wu, S. Zhou, Q. Li, P. Yu, J. Li, W. Duan, and S. Zhou, Phys. Rev. B **105**, L161106 (2022).
[41] D. Eom and J.-Y. Koo, Nanoscale **12**, 19604 (2020).
[42] A. Qu, P. Nigge, S. Link, G. Levy, M. Michiardi, P. Spandar, T. Matthé, M. Schneider, S. Zhdanovich, U. Starke *et al.*, Sci. Adv. **8**, eabm5180 (2022).
[43] M.-H. Zhang, Y.-N. Ren, Q. Zheng, X.-F. Zhou, and L. He, arXiv:2208.01286 (2022).
[44] Y. Mohammadi and S. Bahrami, Chin. Phys. B **31**, 017305 (2022).
[45] E. Andrade, R. Carrillo-Bastos, P. A. Pantaleón, and F. Mireles, J. Appl. Phys. **127**, 054304 (2020).
[46] S. A. Herrera and G. G. Naumis, Phys. Rev. B **101**, 205413 (2020).
[47] S. A. Herrera and G. G. Naumis, Phys. Rev. B **102**, 205429 (2020).
[48] Y. Mohammadi, ECS J. Solid State Sci. Technol. **10**, 061011 (2021).
[49] A. Santacruz, P. E. Iglesias, R. Carrillo-Bastos, and F. Mireles, Phys. Rev. B **105**, 205405 (2022).

[50] J. J. Wang, S. Liu, J. Wang, and J.-F. Liu, Phys. Rev. B **98**, 195436 (2018).

[51] E. Andrade, R. Carrillo-Bastos, and G. G. Naumis, Phys. Rev. B **99**, 035411 (2019).

[52] D. A. Ruiz-Tijerina, E. Andrade, R. Carrillo-Bastos, F. Mireles, and G. G. Naumis, Phys. Rev. B **100**, 075431 (2019).

[53] Q.-P. Wu, L.-L. Chang, Y.-Z. Li, Z.-F. Liu, and X.-B. Xiao, Nanoscale Res. Lett. **15**, 1 (2020).

[54] J. J. Wang, S. Liu, J. Wang, and J.-F. Liu, Phys. Rev. B **101**, 245428 (2020).

[55] W. Zeng and R. Shen, Phys. Rev. B **104**, 075436 (2021).

[56] S. G. y García, T. Stegmann, and Y. Betancur-Ocampo, Phys. Rev. B **105**, 125139 (2022).

[57] E. Andrade, G. G. Naumis, and R. Carrillo-Bastos, J. Phys.: Condens. Matter **33**, 225301 (2021).

[58] H. Ochoa, A. H. Castro Neto, V. I. Fal'ko, and F. Guinea, Phys. Rev. B **86**, 245411 (2012).

[59] C. W. J. Beenakker, Rev. Mod. Phys. **80**, 1337 (2008).

[60] E. McCann and V. I. Fal'ko, J. Phys.: Condens. Matter **16**, 2371 (2004).

[61] D. J. Alspaugh, M. M. Asmar, D. E. Sheehy, and I. Vekhter, Phys. Rev. B **105**, 054502 (2022).

[62] E. Thareja, I. Vekhter, and M. M. Asmar, Phys. Rev. B **102**, 125308 (2020).

[63] M. Tanhayi Ahari, G. Ortiz, and B. Seradjeh, Am. J. Phys. **84**, 858 (2016).

[64] L. Isaev, G. Ortiz, and I. Vekhter, Phys. Rev. B **92**, 205423 (2015).

[65] S. Chen, Z. Han, M. M. Elahi, K. M. Habib, L. Wang, B. Wen, Y. Gao, T. Taniguchi, K. Watanabe, J. Hone *et al.*, Science **353**, 1522 (2016).

[66] M. M. Asmar and S. E. Ulloa, Phys. Rev. Lett. **112**, 136602 (2014).

[67] A. Ferreira, T. G. Rappoport, M. A. Cazalilla, and A. H. Castro Neto, Phys. Rev. Lett. **112**, 066601 (2014).

[68] D. Q. Khoa, C. V. Nguyen, L. M. Bui, H. V. Phuc, B. D. Hoi, N. V. Hieu, V. Q. Nha, N. Huynh, L. C. Nhan, and N. N. Hieu, Mater. Res. Express **6**, 045605 (2019).

[69] S. A. Herrera and G. G. Naumis, Phys. Rev. B **104**, 115424 (2021).